J Mater Sci (2009) 44:4413–4421
DOI 10.1007/s10853-009-3669-3

Structural characteristics and high-temperature oxidation behavior of porous Fe–40 at.%Al alloy

P. Z. Shen · M. Song · H. Y. Gao · Y. H. He · J. Zou · N. P. Xu · B. Y. Huang · C. T. Liu

Received: 20 February 2009 / Accepted: 6 June 2009 / Published online: 23 June 2009

Abstract Porous FeAl alloy was prepared by Fe and Al elemental reaction synthesis. The cyclic oxidation evolutions of porous Fe–40 at.%Al alloy at the elevated temperatures of 600 and 800 °C in air were studied and compared to porous materials of Ti, Ni, and 316L stainless steel. It has been shown that the oxidation of porous Fe–40 at.%Al alloy fitted a power law and no spallation was found after cyclic oxidation for 202 h in air. The porous FeAl alloy exhibits much better oxidation resistance than other porous materials, such as Ti, Ni, and 316L stainless steel, indicating that the porous Fe–40 at.%Al alloy has the highest structural stability at the elevated temperature in the oxidation atmosphere. Thus, the porous FeAl alloy can be used as filtering materials at elevated temperature in the oxidation atmosphere.

P. Z. Shen · M. Song · H. Y. Gao · Y. H. He (✉) · B. Y. Huang
State Key Laboratory for Powder Metallurgy, Central South University, Changsha 410083, China
e-mail: yuehui@mail.csu.edu.cn

J. Zou (✉)
School of Engineering and Centre for Microscopy and Microanalysis, The University of Queensland, Brisbane, QLD 4072, Australia
e-mail: j.zou@uq.edu.au

N. P. Xu
Membrane Science and Technology Research Center, Nanjing University of Technology, Nanjing 210009, China

C. T. Liu
Department of Mechanical Engineering, The Hong Kong Polytechnic University, Hong Kong, China

Introduction

High temperature industrial processes commonly give rise to dusts which need to be removed before the product gases are discharged to the atmosphere. The most efficient way of separating particles at high temperature is to use filters [1]. Inorganic porous materials (porous ceramics and porous metals) possess some inherent advantages over the organic ones, such as superior mechanical stability, cleaning ability, and long life [2–4]. However, the disadvantages of porous ceramics (the brittleness, poor weldability, and poor thermal shock resistance [5]) and porous metals (the poor oxidation/corrosion resistance [6]) have limited their practical applications at high temperatures.

FeAl intermetallics are provided with the advantages of metals and ceramics due to co-existence of the covalent bonds and metallic bonds in the crystal structure, offering a combination of properties such as the excellent oxidation/sulfidation resistance, light weight, and economical cost advantages over the conventional high temperature materials [7–9]. For this reason, it is of interest to fabricate porous FeAl alloys to be used at elevated temperatures as cellular filters. Previous studies [10, 11] indicated that porous FeAl alloys can be synthesized by pre-formed FeAl powders and SHS (self-propagation high-temperature synthesis) technique. However, the disadvantages of the pre-formed powder method (complex process, poor formability, and sintering property of pre-formed powder, and oxide dispersion in FeAl pre-formed powders [12]) and SHS method (poor controllability of the shape and pore structures) have limited their fabricability. Our recent studies [13–15] have demonstrated that near-net-shape porous TiAl and FeAl alloys can be fabricated through reactive syntheses of commercial Fe and Al or Ti and Al mixed powders based on the Kirkendall effect. This

method has many advantages, such as economical cost, excellent formability, fabricating shape-complex work piece, modifying the composition based on the requirement, enabling near-net shape, and large-scale adjusting of pore structures.

Considerable researches show that block Fe–Al intermetallics have excellent oxidation resistance at elevated temperatures due to the formation of Al_2O_3 on the surfaces, as a result of selective oxidation of aluminum [16, 17]. Although the decisive factor of corrosion resistance is molecular structure of the materials, the related mechanisms on the oxidation of dense material should not be simply applied to the porous materials, since the pore structure and related material parameters can modify the kinetics and the adherence between the oxide scale and the substrate during oxidation [18–20]. Moreover, stability of pore structure should be considered as a key parameter for porous material working at elevated temperature, which determines the working life and filtered precision of the porous materials. In this study, porous Fe–40 at.%Al intermetallics, the most classical composition in Fe–Al alloys, was investigated to evaluate the oxidation behavior at 600 and 800 °C, which may be considered as a reliable assessment for the potential applications at high temperatures.

Experimental details

Elemental powders of iron (99.8% purity carbonyl powders with the average particle diameter of 3 $\sim$ 5 μm) and aluminum (99.5% purity gas atomized powders with the average particle diameter of 3 $\sim$ 5 μm) were blended with a suitable proportion (40 at.%Al) and homogenized in a cylinder mixer, and then cold pressed uniaxially to form a compact disc with a dimension of Φ 32 $\times$ 2 mm^2 under a pressure of 250 MPa. No binder and lubricant were added during the process due to good formability of Fe and Al mixed powders. The compact discs were then sintered in a vacuum furnace with a pressure of 10^{-3} Pa. The compact discs were initially heated to 550 °C with a heating rate of 10 °C min^{-1}, and kept at 550 °C for 1 h; then the discs were further heated to 640 °C with a heating rate of 1 °C min^{-1}, and kept at 640 °C for 1 h. Subsequently, the compact discs were heated to 1050 °C with a heating rate of 5 °C min^{-1} and held at this temperature for 1 h. The sintered discs were then cooled inside the furnace to the room temperature. To compare with the properties of porous FeAl alloys, popular porous metals (such as Ti, Ni, and 316L stainless steel) were also synthesized by the powder metallurgy technique [21].

All specimens were ultrasonically cleaned and degreased using acetone, dried and accurately weighed in a balance with a accuracy of ±0.1 mg. The samples placed in crucibles were introduced in the furnace and kept at two different temperatures (600 and 800 °C) in air during cyclic oxidation. After air cooling to the room temperature, the surface area, weight change, and pore structural parameters of the sintered discs were measured before returning to the furnace. A total oxidation time is 202 h during cyclic oxidation.

The pore size distribution of porous Fe–40 at.%Al alloy was measured by mercury porosimetry (Poremaster GT-60, Quantachrome). Surface areas of all specimens were measured using Brunauer-Emmett-Teller (BET) method (Monosorb, Quantachrome). Oxidation products were identified using X-ray diffraction method (XRD, D/MAX-RA). The surface morphology and fractured sections of the oxidized specimens were investigated using a scanning electron microscopy [SEM, LEO1525 equipped with energy-dispersive X-ray (EDX) system for chemical analysis]. Cross-sectional specimens were prepared using conventional metallographic techniques, without polishing agent to avoid possible confusion with the oxidation products. The open porosity was measured by the Archimedes method, and the maximum pore size was determined through the bubble point method [22, 23]. Tensile strength and fracture toughness of the specimen were tested on the mechanical testing machine (LJ-3000A) with a strain rate of 1 $\times$ 10^{-3} s^{-1}. The detailed testing method of mechanical properties can be found in Ref. [24]. A Netzsch DIL 402C was used for the thermal expansion measurements. Samples for the thermal expansion experiment were 3 mm in diameter and 20 mm in length and the compression load during the measurement was 25 N.

Results

Characterization of the initial porous Fe–40 at.%Al alloy

Figure 1 shows the XRD patterns of the compact discs before and after the sintering process. The diffraction peaks in the XRD patterns of the as-pressed disc (Fig. 1a) can be fully indexed by elemental Fe and Al, while the diffraction peaks in the XRD patterns of the sintered compact disc (Fig. 1b) can be completely indexed by the Fe–Al B2 structure, suggesting that the sintering has promoted a complete phase transformation (Fe + Al → Fe – Al).

Figure 2 shows the SEM images of the surfaces of the compact discs before and after the sintering. It can be seen that the powdered morphology (Fig. 2a) changes to the porous morphology (Fig. 2b) after sintering. The reactive pores are distributed uniformly in macro-scale, but non-uniformly in micro-scale, due to the aggregation of Al

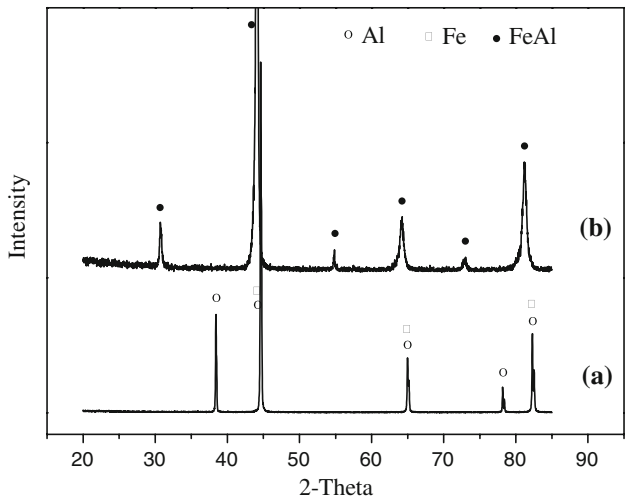

Fig. 1 XRD patterns of the as-pressed compact (**a**) and sintered compact at 1050 °C (**b**)

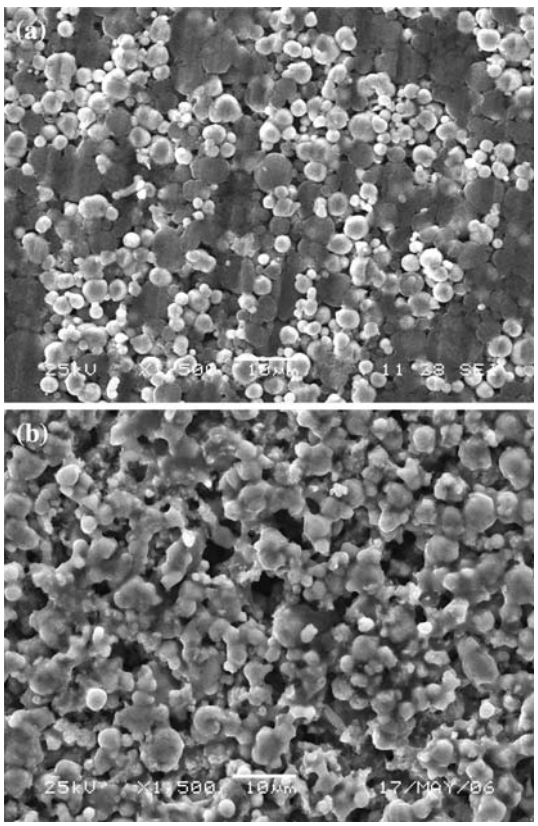

Fig. 2 SEM images showing the microstructures of the as-pressed compact disc (**a**) and sintered compact disc (**b**)

powders with average sizes of 3 ~ 5 μm and the clearance pore in the as-pressed compact discs. It was also found that these pores are open pores, evidenced by the gas permeability measurement. The pore formation is attributed to the Kirkendall effect [13–15].

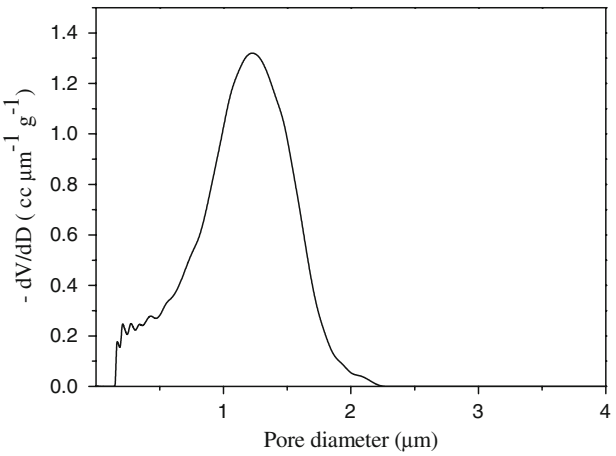

Fig. 3 Pore diameters distribution of porous Fe–40 at.% alloy

Figure 3 shows pore-size distribution of the porous Fe–40 at.%Al alloy. The sample has a narrow pore size distribution, ranging from 0.2 μm to 2.3 μm with a center at 1.4 μm. The gas permeability is 3.44 $m^3\ m^{-2}\ kPa^{-1}\ h^{-1}$. The tensile strength and fracture toughness of porous Fe–40 at.%Al alloy were determined to be 91.99 MPa and 3.9 MPa $m^{1/2}$, respectively.

Oxidation behavior of porous Fe–40 at.%Al alloy at elevated temperatures

Figure 4 shows the variation of the specific surface area as a function of the oxidation duration at 600 and 800 °C, respectively. It can be seen that after a rapid decrease in the first 10 h, the remaining change of the surface area tends to be small in the rest oxidation process. The surface area of porous Fe–40 at.%Al alloy changes from 0.26 $m^2\ g^{-1}$ to 0.16 and 0.18 $m^2\ g^{-1}$ after 92 h in cyclic oxidations at 600 and 800 °C, respectively. After 92 h, the surface area remains stable at both temperatures and is much larger than

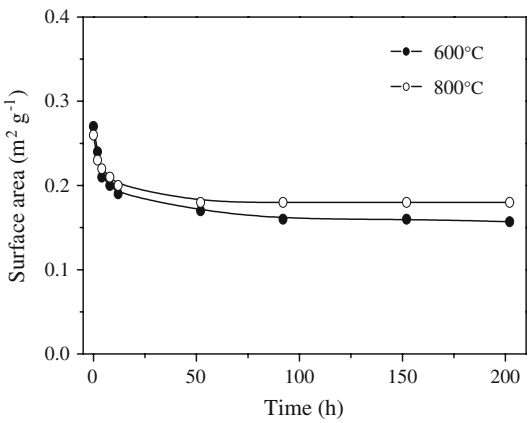

Fig. 4 Surface area as a function of time for the oxidation of porous Fe–40 at.%Al alloy at 600 and 800 °C

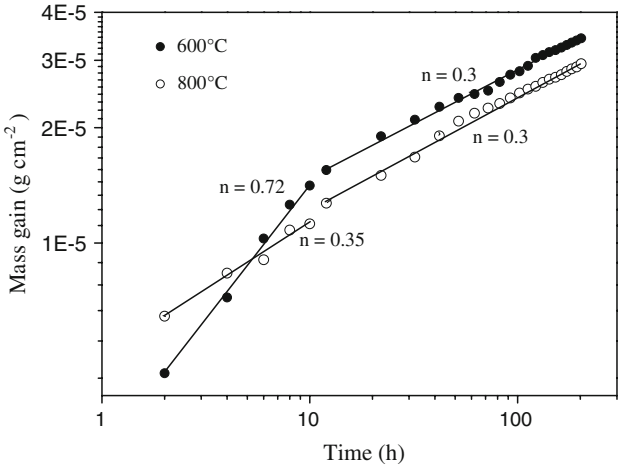

Fig. 5 Variation of the average values of mass gain per unit surface area during oxidation at 600 and 800 °C as a function of exposure time for the porous Fe–40 at.%Al alloy

the surface area of the comparative dense alloy with the same size and shape. This indicates that a large number of pores retain in the porous FeAl alloy.

Figure 5 shows the variation of the mass gain during the oxidation as a function of the exposure time in a double logarithmic plot. The plots are smooth, indicating a good layer/alloy adherence during oxidation at 600 and 800 °C. The mass gain per unit surface area was fitted to a power law of $\left(\Delta m/A\right) = kt^{n}$, where Δm is the mass change due to oxidation, A is the area of the sample subjected to oxidation atmosphere, k is the oxidation rate constant, n is the rate exponent, and t is the oxidation time. In Fig. 5, two stages are clearly observed for each case. The rate exponent is 0.72 and 0.35 for the first 10 h of oxidation at 600 and 800 °C, respectively, while it is 0.3 after 10 h at both temperatures.

Evolution of pore parameters of porous Fe–40 at.%Al alloy during oxidation process

In generation, the oxide layer increases with increasing the oxidation time, which affects the pore parameters of porous materials during the oxidation process. To understand the stability of pore parameters (the maximum pore size and the permeability) of various porous materials during the oxidation process, the pore parameters of current popular porous Ti, Ni, 316L stainless steel and porous Fe–40 at.%Al alloys were compared under the same oxidation process.

The maximum pore size not only indicates the accuracy of the filter (the largest particle can pass the filter), but also evaluates the average pore size due to determined relation between the average pore size d and the maximum pore size d_m with $d = Ad_m$, where A is the proportion factor [14].

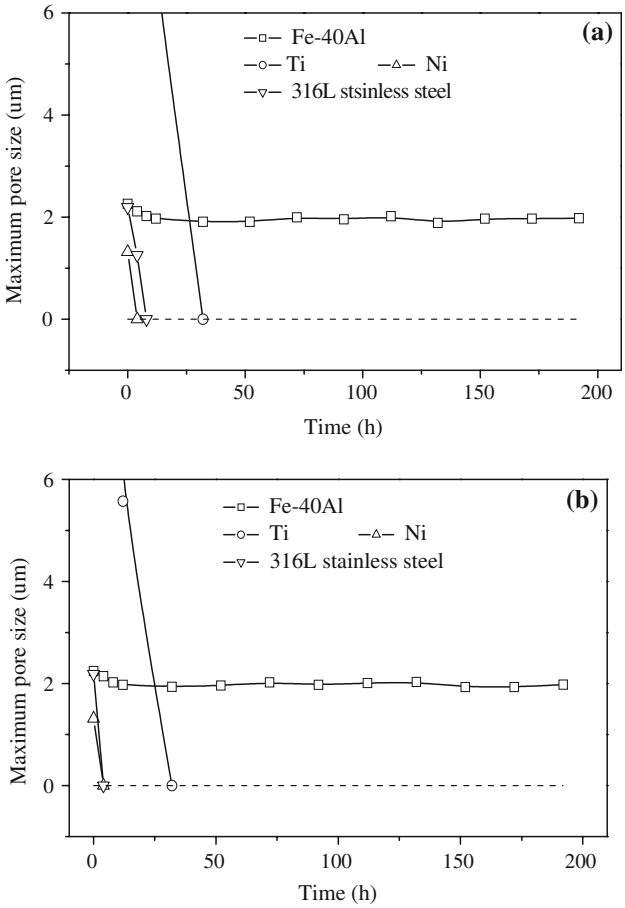

Fig. 6 Maximum pore size as a function of oxidation time for porous Fe–40 at.%Al, Ti, Ni, and 316L stainless steel materials oxidized in air at **a** 600 °C and **b** 800 °C

Figure 6 shows the maximum pore sizes of the tested porous materials as a function of the oxidation time during the oxidation processes at 600 and 800 °C, respectively. It can be seen in Fig. 6a (the case oxidized at 600 °C) that the maximum pore sizes of porous Ni, 316L stainless steel, and Ti decrease sharply with the oxidation time and change to zero after only 4, 8, and 32 h of oxidation, respectively. However, the maximum pore size of porous Fe–40 at.%Al alloy only decrease slightly from 2.3 μm to 2.0 μm in the first ~32 h of oxidation and then remains stable for the rest of the oxidation process. A similar tendency can also be observed when the oxidation was carried out at 800 °C (Fig. 6b).

Since the permeability is another key pore parameter to evaluate porous materials, the influence of the oxidation time on the permeability of porous Ti, Ni, 316L stainless steel and porous Fe–40 at.%Al alloy was also studied and the results are shown in Fig. 7. Similar to the maximum pore size, porous Ni, 316L stainless steel, and Ti are not permeable after the first 4, 8, and 32 h, respectively. However, for the porous Fe–40 at.%Al alloy, the

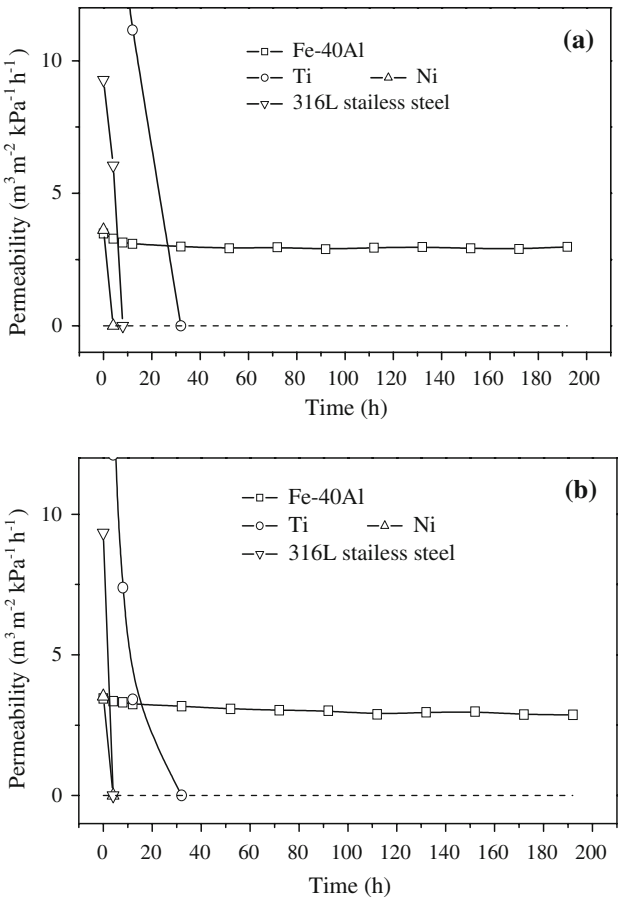

Fig. 7 Permeability versus oxidation time for porous Fe–40 at.%Al, Ti, Ni, and 316L stainless steel material oxidized in air at **a** 600 °C and **b** 800 °C

permeability decreases only from 3.4 $m^3\ m^{-2}\ kPa^{-1}\ h^{-1}$ to 3.0 $m^3\ m^{-2}\ kPa^{-1}\ h^{-1}$ in the first ~32 h, then remains stable at both temperatures. The fact that a large number of open pores are retained in the porous Fe–40 at.%Al alloys after high temperature oxidation clearly suggests that porous Fe–40 at.%Al alloy can be used for the filter applications at high temperature due to their excellent stability of pore parameters and oxidation resistance.

Structural characterization of oxidized porous Fe–40 at.%Al alloy

Figure 8 shows XRD patterns of porous Fe–40 at.%Al alloy oxidized at 600 and 800 °C for 202 h, respectively. Compared to the non-oxidized case (Fig. 1b), in which only the FeAl B_2 structure was observed, some additional weak diffraction peaks near $2\theta = 35$, 43.5, and 57.5° can also be observed, which fit well with the diffraction peaks of α-Al_2O_3, suggesting that α-Al_2O_3 is the major phase formed during the oxidation process. The additional diffraction peaks are relatively weak compared with the FeAl

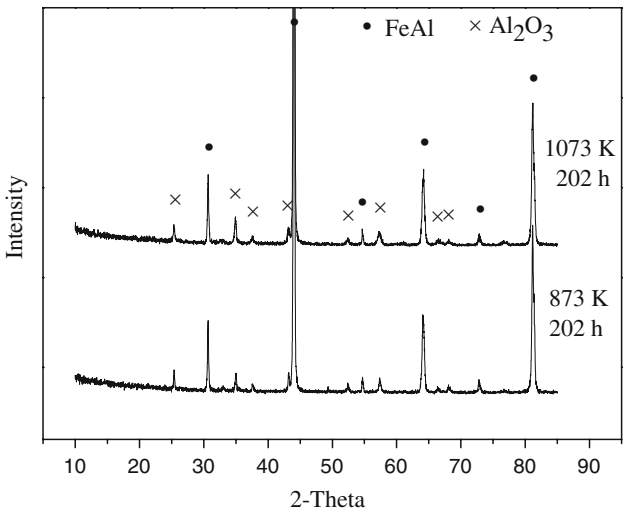

Fig. 8 X-ray diffraction patterns of the surface of the porous Fe–40 at.%Al alloy oxidized at different temperatures

B_2 diffraction peaks, indicating that the thickness of Al_2O_3 is very thin.

Figure 9 shows the surface morphology of porous Fe–40 at.%Al alloy, porous Ti, Ni, and 316L stainless steel after high temperature oxidation. It can be seen from Fig. 9a and b that the pores can still be remained on the surface of Fe–40 at.%Al alloy after oxidation at 600 and 800 °C for 202 h. However, for porous Ti, Ni, and 316L stainless steel oxidized at 600 °C for 32 h, oxide layer forms on their outer surface and gas permeability measurement shows the pores are blocked.

Cross-sections of the porous Fe–40 at.%Al alloy oxidized at 600 and 800 °C for 202 h were studied using SEM and the results were presented in Fig. 10. It can be seen that the connected open pore structures exist in the porous FeAl alloy after the oxidation process. To further confirm the oxide layer on the internal surface, energy-dispersive spectroscopy (EDS) analysis was used to determine the chemical composition of bulk regions (location 1) and internal surface (location 2) for both cases. It can be clearly seen that location 1 only shows the elements of Fe and Al, while location 2 shows the existence of oxygen. When combined with XRD, we can determine that Al_2O_3 is formed on the surface (including internal surface) of the porous Fe–40 at.%Al alloys during the high temperature oxidation process.

Discussion

It is well known that dense Fe–40Al alloy can only form an external Al_2O_3 layer by the selective oxidation of Al. The presence of aluminum oxide results from surface diffusion, including the outward diffusion of Al (the major transport

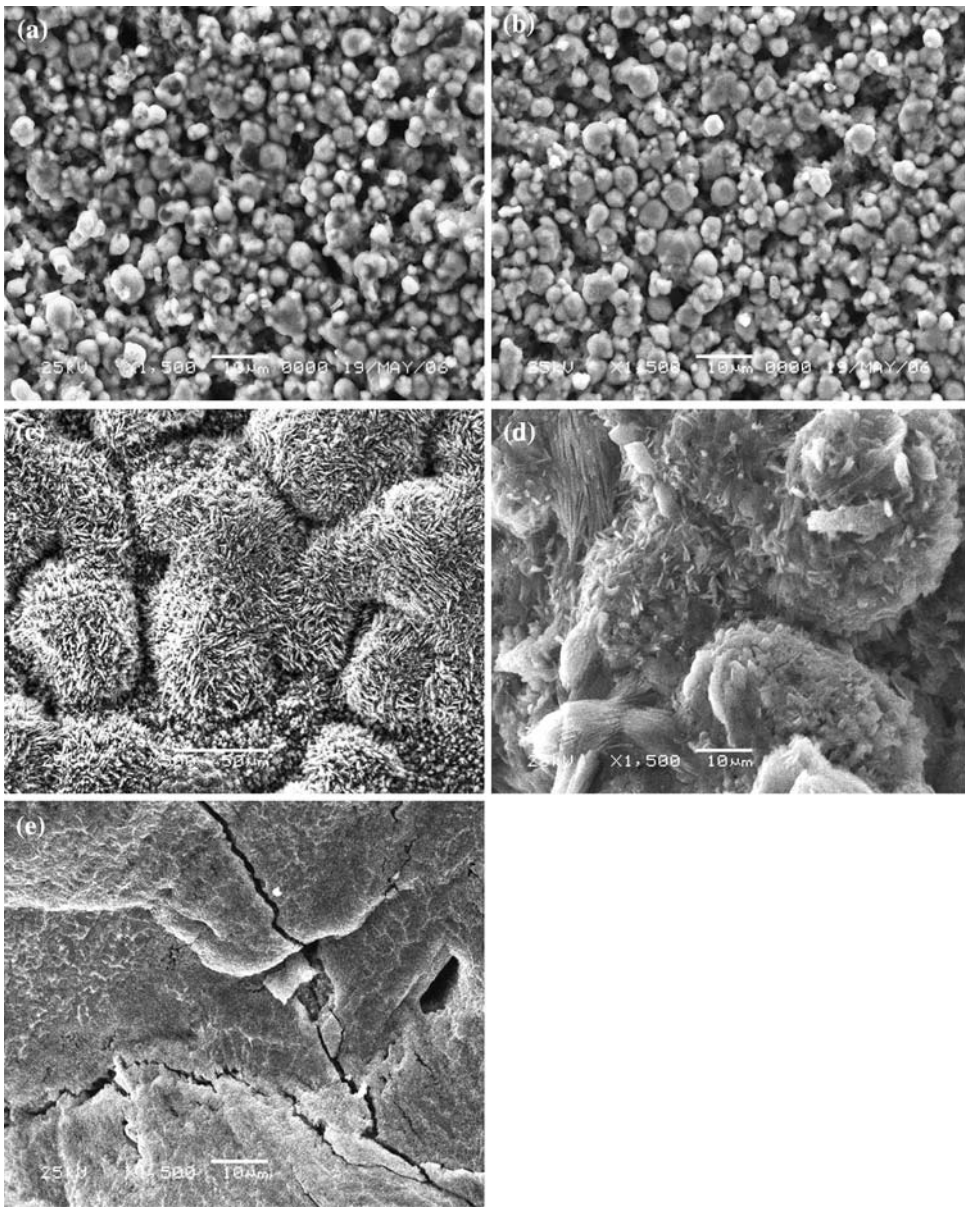

Fig. 9 Surface morphologies of porous materials after oxidation. **a** porous Fe–40 at.%Al at 600 °C for 202 h, **b** Fe–40 at.%Al at 800 °C for 202 h, **c–e** porous Ti, Ni, and 316L stainless steel at 600 °C for 32 h, respectively

mode) and the inward diffusion of oxygen using short circuit diffusion paths [25]. For the porous material, connecting open pores promote fast inward transport of air by gaseous diffusion, and, in turn, Al_2O_3 forms due to selective oxidation of Al.

It should be noted that the rate exponents decrease for porous FeAl alloy during oxidation at both temperatures, as shown in Fig. 5, which might result from the initial formation of metastable alumina [25, 26]. It is well known that transition alumina is a fast growing oxide compared to α-alumina, leading to less protective layers. It transforms to more stable α-alumina, and then further oxidation reaction would be partially protected. Therefore, the rate exponent decreases during further oxidation. In addition, the metastable alumina transforms rapidly to α-alumina at 800 °C during the first 10 h of oxidation, which results in the mass gain at 800 °C being lower than that at 600 °C. Therefore, the rate exponent at 800 °C is somewhat lower that that at 600 °C in the first 10 h of oxidation. Similarly, surface area of the porous FeAl alloy oxidized at 800 °C is higher than that oxidized at 600 °C due to the inverse relationship between the mass gain and the surface area.

Montealegre et al. [26] have also found a rate exponent of 0.3 on the oxidation behavior of Fe–40 at.%Al alloy strip of 200 μm thick. Compared to the classic formula, $\left(\Delta m/A\right) = kt^{0.5}$, the difference in the oxidation kinetics probably results from the smaller number of grains in specific area in porous material or strip than that in bulk FeAl, which affects the diffusion flow during high temperature oxidation and modifies the oxidation kinetics.

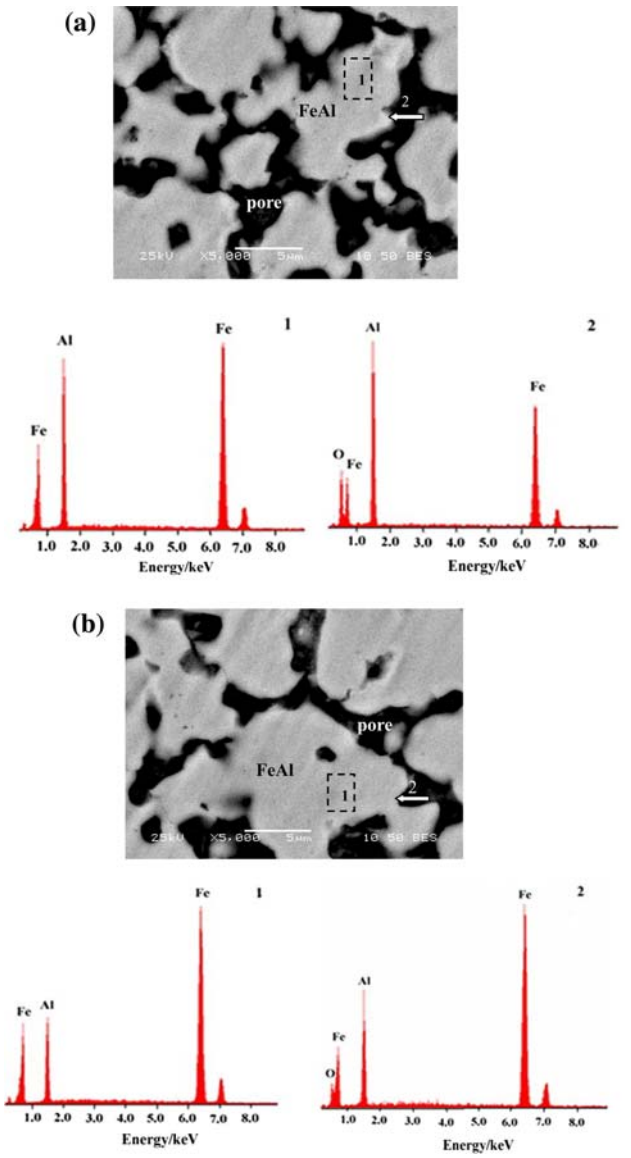

Fig. 10 Backscattered electron image showing the cross-sectional view of the porous Fe–40 at.%Al alloy after oxidation at different temperature for 202 h, **a** 600 °C **b** 800 °C

For porous materials, the stability of pore structure is related to characteristics of oxide layer and adherence between the oxide layer and the substrate during the oxidation. The oxide layer of porous Ti and porous Ni is loose, as shown in Fig. 9c and d, thus O_2 can further react with the substrate. For the 316L stainless steel, the $(Fe, Cr)_2O_3$ layer allows fast outward transport of Fe by diffusion [27, 28], and the crack initiation by thermal stress, as shown in Fig. 9f, allows fast inward transport of oxygen by gas diffusion, leading to further oxide reaction. Therefore, an increased amount of oxide would clog the pore in the porous materials. As a result of that, the values of pore structural parameters would decrease sharply, and then filtering would stop. However, for the porous FeAl alloy, the dense Al_2O_3 layer caused by the selective oxidation of Al can avoid further oxidation. Adhesion between Al_2O_3 layer and porous FeAl alloy can be discussed as follows.

No spallation of oxide layer has been observed during the cyclic oxidation process for porous Fe–40 at.%Al alloy, compared to the dense bulk alloys with similar compositions [17, 29]. Even the dense bulk alloy containing 1% yttria (known as efficient in suppressing the layer spallation) is prone to spallation unless a slow cooling is applied after the oxidation [30]. Under the cyclic oxidation conditions, the sample bears growth stress and thermal stress. For the porous FeAl alloys, the growth stress mainly includes two groups—bulk stress and shape stress [31]. Bulk stress is caused by the change of volume from metal to oxide, which can be calculated by the following equation: $PBR = V_{ox}/V_m$, where V_{ox} and V_m are the volumes of the generated oxide and of the lost metal for generating oxide, respectively. $PBR = 1$ is zero-bulk-stress status, $PBR > 1$ indicates compressive stress in the oxide layer and tensile stress in the substrate. Previous study indicated that $PBR = 1.28$ for Al/Al_2O_3 system [32]. The shape stress is generated by the geometrical shape of oxidized specimen. On an ideal surface, the shape stress has no effect on oxide growth. Figure 11 illustrates the shape stress state of two typical oxide layers. During the oxidation, outer diffusion of Al on the convexity leads to inward shrink of metal interface, resulting in the compressive stress developed at the neighboring oxide layer. Meanwhile, an inward flux of oxygen leads to tensile stress developed at the neighboring oxide layer. On the other hand, outer diffusion of Al and inward flux of oxygen on the concavity lead to compressive stress developed at the neighboring oxide layer. The above-mentioned stresses state simultaneously exists due to the rough surface of particles (Fig. 10a). In addition, since the frame of the porous alloy is formed by particles being smaller than 10 μm, plastic deformation can easily appear to relieve the stress concentration. Therefore, the growth stress is considered not high enough to cause the formation of layer spallation, so its effect can be ignored during the oxidation.

Thermal stress derives from the difference in thermal expansion coefficient between the oxide and the substrate. Figure 12 shows the thermal expansion curve of the porous Fe–40 at.%Al alloy. The thermal expansion coefficients from room temperature to 600 and 800 °C are 22.0629×10^{-6} °C^{-1} and 21.2470×10^{-6} °C^{-1}, respectively; a little less than that of dense Fe–40 at.%Al alloy (22.7×10^{-6} °C^{-1}) [33] due to the existence of pores [34]. At the cooling stage, the oxide layer bears compressive stress and the substrate bears tensile stress because the thermal expansion coefficient of Fe–40 at.%Al is much higher than that of α-Al_2O_3 (8.1×10^{-6} °C^{-1}) [35]. For

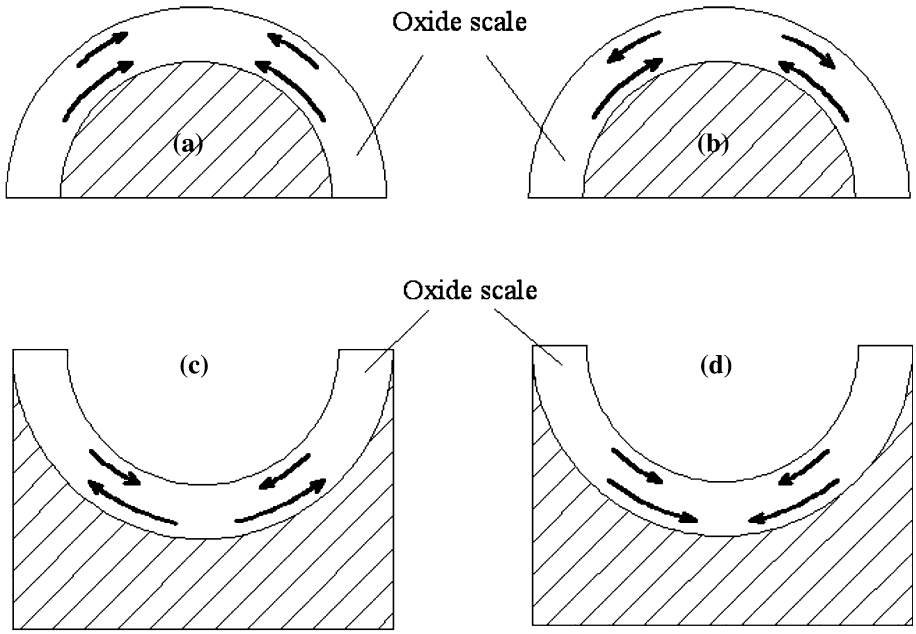

Fig. 11 Illustration of shape stress state in the scale and the porous alloy during thermal cyclic oxidation, **a** cationic diffusion on the convexity, **b** anionic diffusion on the convexity, **c** cationic diffusion on the concavity, **d** anionic diffusion on the concavity

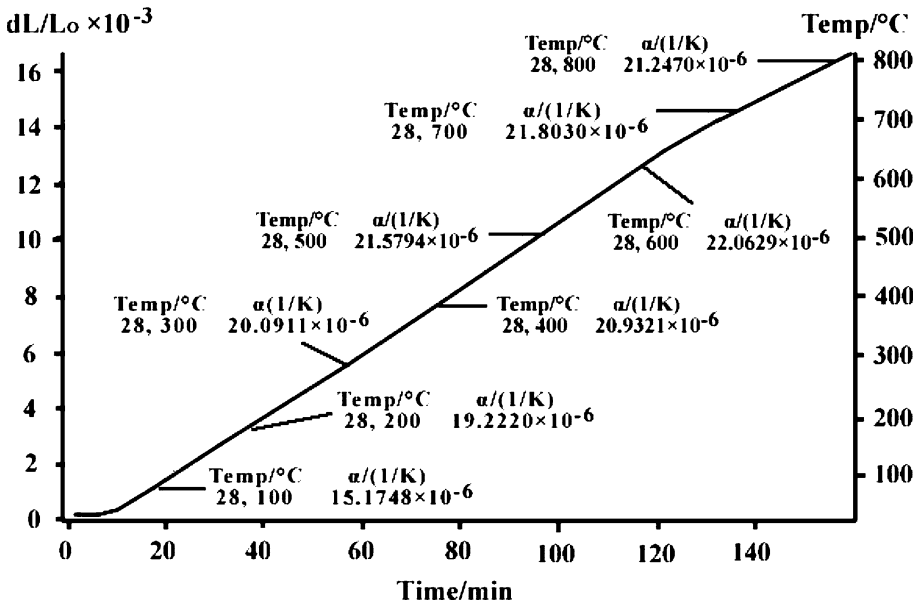

Fig. 12 Thermal expansion curve of porous Fe–40 at.%Al alloy

dense Fe–40 at.%Al alloys, spallation happens because the layer cannot withstand the elevated compressive stresses during the cooling [17]. The absence of spallation on the porous Fe–40 at.%Al alloy can be understood as follows. The tensile strength of porous Fe–40 at.%Al alloys (91.99 MPa) is far lower than that of dense Fe–40 at.%Al (the tensile strength of Fe–40 at.%Al sheet is about 660 MPa) [36]. This indicates that the stress relaxation is easier in the porous Fe–Al alloy than in the Fe–40 at.%Al. In addition, since the frame of the porous alloy is formed by particles being smaller than 10 μm, plastic deformation easily appears to relieve the stress. As a result, no spallation occurs in porous Fe–40 at.%Al alloy.

Conclusions

Fe–40 at.%Al porous alloy was successfully fabricated with an excellent oxidation resistance, tested in the cyclic oxidation for 202 h in air at 600 and 800 °C. Pore structure curve for the cyclic oxidation at elevated temperature reveals that porous Fe–40 at.%Al alloy can retain filtration

capacity and possesses higher stability of pore structure at elevated temperature in oxidation atmosphere than the porous materials of Ti, Ni, and 316L stainless steel.

Acknowledgements This research was performed under the auspices of National Basic Research Program of China (No. 2009CB623400), National Natural Science Foundation of China (No.20476106 and No.20636020), National Natural Science Founds for Distinguished Young Scholar (No.50825102) and the 111 Project of Chinese Ministry of Education.

References

1. Davis TW (2000) Air pollution engineering manual. Wiley, Canada
2. Chae SH, Kim YW (2009) J Mater Sci 44:1404. doi:10.1007/s10853-009-3264-7
3. Qiu MH, Feng J, Fan YQ, Xu NP (2009) J Mater Sci 44:689. doi:10.1007/s10853-008-3202-0
4. Hsieh HP (1996) Inorganic membrane for separation and reaction. Elsevier Science B V, New York
5. She JH, Ohji T (2002) J Am Ceram Soc 85:2125
6. Liu PS, Liang KM (2001) J Mater Sci 36:5059. doi:10.1023/A:1012483920628
7. Deevi SC, Sikka VK, Liu CT (1997) Prog Mater Sci 42:177
8. Guilemany JM, Cinca N, Casas L, Molins E (2009) J Mater Sci 44:2152. doi:10.1007/s10851-009-3296-z
9. Stoloff NS, Liu CT, Deevi SC (2000) Intermetallics 8:1313
10. Pang HJ, Ye YF, Chen B (2006) Heat Treat Met 31:55
11. Ranganath S, Prakash TL, Subrahmanyam J (1990) Mater Lett 10:215
12. Godlewska E, Szczepanik S, Mania R, Krawiarz J, Kozinski S (2003) Intermetallics 11:307
13. He YH, Jiang Y, Xu NP, Zou J, Huang BY, Liu CT, Liaw PK (2007) Adv Mater 19:2102
14. Jiang Y, He YH, Xu NP, Zou J, Huang BY, Liu CT (2008) Intermetallic 16:327
15. Gao HY, He YH, Shen PZ, Xu NP, Zou J, Jiang Y, Huang BY, Liu CT (2008) Powder Metall 51:171
16. Saunders SRJ, Monteiro M, Rizzo F (2008) Prog Mater Sci 53:775
17. Almathami A, Elhachmi E, Brochu M (2008) J Mater Sci 43:3452. doi:10.1007/s10853-008-2517-1
18. Bull SJ (1998) Oxid Met 49:1
19. Messaoudi K, Huntz AM, Menza LD (2000) Oxid Met 53:49
20. Klinger L, Rabkin E, Shvindlerman LS, Gottstein G (2008) J Mater Sci 43:5068. doi:10.1007/s10853-008-2678-y
21. Lin XQ, He YH, Jiang Y, Zhang FS (2005) Mater Sci Eng Powder Metall 10:127
22. German RM (1994) Powder metallurgy science. Metal Powder Industries Federation, Princeton, p 370
23. Kim H, Han Y, Park J (2009) Mater Charact 60:14
24. Czichos H, Saito T, Smith L (2006) Springer handbook of measurement methods for materials properties. Springer Science + Business Media, Inc, New York
25. Chan CDN, Huvier C, Dinhut JF (2001) Intermetallics 9:817
26. Montealegre MA, Gonzalez-Carrasco JL, Mun oz-Morris MA (2001) Intermetallics 9:487
27. Molin S, Gazda M, Kusz B, Jasinski P (2008) J Eur Ceram Soc. doi:10.1016/j.jeurceramsoc.2008.07.027
28. Li MS (2001) High temperature corrosion of metals. Metallurgical Industry Press, Beijing
29. Montealegre MA, Gonzalez-Carrasco JL, Morris-Munoz MA, Chao J, Morris DG (2000) Intermetallics 8:439
30. Rao VS, Baligidad RG, Raja VS (2002) Intermetallics 10:73
31. Qu HL, Zhou L, Wei HR, Zhao YQ (2001) Chinese J Nonferrous Met 11:398
32. Zhai JK (1994) High temperature corrosion of metals. Beijing Aeronautic and Astronautics University Press, Beijing, p 60
33. Deevi SC (2000) Intermetallics 8:679
34. Novikov VV (1983) J Eng Phys 44:660
35. Lang FQ, Yu ZM, Gedevanishvili S, Deevi SC, Narita T (2004) Intermetallics 12:451
36. Deevi SC, Swindeman RW (1998) Mater Sci Eng A 258:203